This is a preprint, the final version is subject to change, of the American Mineralogist (MSA)
Cite as Authors (Year) Title. American Mineralogist, in press.
(DOI will not work until issue is live.) DOI: http://dx.doi.org/10.2138/am-2017-5881

Revision 1

Formation of phosphorus-rich olivine in Dar al Gani 978 carbonaceous chondrite through fluid-assisted metamorphism

YANG LI[1], AI-CHENG ZHANG[1,2,*], JIA-NI CHEN[1], LI-XIN GU[3], AND RU-CHENG WANG[1]

[1]State Key Laboratory for Mineral Deposits Research, School of Earth Sciences and Engineering, Nanjing University, Nanjing 210046, China

[2]Lunar and Planetary Science Institute, Nanjing University, Nanjing 210046, China

[3]Institute of Geology and Geophysics, Chinese Academy of Sciences, Beijing 100029, China

*E-mail: aczhang@nju.edu.cn

This is a preprint, the final version is subject to change, of the American Mineralogist (MSA)
Cite as Authors (Year) Title. American Mineralogist, in press.
(DOI will not work until issue is live.) DOI: http://dx.doi.org/10.2138/am-2017-5881

16 # ABSTRACT

17 Phosphorus-rich olivine (P_2O_5 > 1 wt%) is a mineral that has been reported only in a
18 few terrestrial and extraterrestrial occurrences. Previous investigations suggest that P-rich
19 olivine mainly forms through rapid crystallization from high-temperature P-rich melts.
20 Here, we report a new occurrence of P-rich olivine in an ungrouped carbonaceous
21 chondrite Dar al Gani (DaG) 978. The P-rich olivine in DaG 978 occurs as lath-shaped
22 grains surrounding low-Ca pyroxene and olivine grains. The lath-shaped olivine shows a
23 large variation in P_2O_5 (0–5.5 wt%). The P-rich olivine grains occur in a chondrule
24 fragment and is closely associated with chlorapatite, merrillite, FeNi metal, and troilite.
25 Tiny Cr-rich hercynite is present as inclusions within the P-rich olivine. The lath-shaped
26 texture and the association with Cr-rich hercynite indicates that the P-rich olivine in DaG
27 978 formed by replacing low-Ca pyroxene precursor by a P-rich fluid during a thermal
28 event, rather than by crystallization from a high-temperature melt. The large variation of
29 P_2O_5 within olivine grains on micrometer-scale indicates a disequilibrium formation
30 process of the P-rich olivine. The occurrence of P-rich olivine in DaG 978 reveals a new
31 formation mechanism of P-rich olivine.

32 **Keywords**: phosphorus-rich olivine; fluid-assisted metamorphism; Dar al Gani 978;
33 carbonaceous chondrite

INTRODUCTION

Olivine is a common mineral in terrestrial igneous rocks and extraterrestrial materials. Most natural olivine grains contain very low concentrations of P_2O_5 due to a low partition coefficient for P between olivine and melt (<0.1, Anderson and Greenland 1969; Brunet and Chazot 2001; Milman-Barris 2008; Boesenberg and Hewins 2010). Despite its extreme rarity in nature, several occurrences of P-rich olivine (P_2O_5 > 1 wt%) have been reported in a few terrestrial and extraterrestrial samples, with various geological settings. In terrestrial samples, P-rich olivine has been reported in three different settings (Goodrich 1984; Agrell et al. 1998; Tropper et al. 2004; Schneider et al. 2013). First, Goodrich (1984) described dendritic P-rich olivine (0.2–2.7 wt% P_2O_5) within silicate inclusions in an iron-carbon alloy from Disko land, West Greenland. It was suggested that this P-rich olivine is a result of rapid crystallization from supersaturated liquids under the chemical condition of high P_2O_5 contents coupled with low SiO_2 contents, low fO_2 (Goodrich 1984). Second, Agrell et al. (1998) reported P-rich olivine with a P_2O_5 content up to 6.1 wt% from two samples from the Pine Canyon breccia pipe, Utah. The exact formation mechanism of this P-rich olivine remains unknown due to lack of outcrop source of its host rock (Agrell et al. 1998). The authors favored a disequilibrium formation mechanism for the P-rich olivine and interpreted that high P_2O_5 content and low silica activity are responsible for the formation of P-rich olivine. The third occurrence of P-rich olivine in terrestrial samples was found in two prehistoric ritual

54 immolations in Tyro, Austria (Tropper et al. 2004; Schneider et al. 2013). These P-rich
55 olivine grains are closely associated with phosphate minerals, containing up to 23 wt%
56 P_2O_5. It was suggested that the formation of these P-rich olivine grains are related to
57 partially melting and rapid, non-equilibrium crystallization of the precursor rocks with
58 incorporation of chlorapatite, which supplied the phosphorus (Tropper et al. 2004;
59 Schneider et al. 2013).

60 Two types of occurrences of P-rich olivine have been reported in extraterrestrial
61 samples (Buseck 1977; Buseck and Clark 1984; Wasson 1999; Sonzogni et al. 2009;
62 Fowler-Gerace and Tait 2015; Wang et al. 2007). One is P-rich olivine (2-32 wt% P_2O_5)
63 in pallasite meteorites (Buseck 1977; Buseck and Clark 1984; Wasson 1999; Sonzogni et
64 al. 2009; Fowler-Gerace and Tait 2015). Buseck (1977) suggested that the formation of
65 P-rich olivine in pallasite meteorites should be due to replacement reaction with adjunct
66 phosphates below the solidus. Recently, however, Fowler-Gerace and Tait (2015)
67 proposed that the P-rich olivine in pallasite formed by extremely rapid crystallization
68 from a melt. The other extraterrestrial P-rich olivine (0.2–3.9 wt% P_2O_5) was described in
69 the altered opaque assemblages from the Ningqiang carbonaceous chondrite (Wang et al.
70 2007). Wang et al. (2007) inferred that this P-rich olivine might have formed by
71 non-equilibrium reaction between P-bearing molten metal and olivine crystals during
72 rapid cooling. In summary, most of the natural P-rich olivine grains seems to be due to
73 rapid crystallization from high-P and low-Si melts, although the olivine from the Pine

Canyon breccia pipe, Utah might have a different origin. This scenario was enhanced recently by the experimental investigation by Boesenberg and Hewins (2010) on P-rich olivine and by Fowler-Gerace and Tait (2015). The latter excluded the subsolidus origin of P-rich olivine in pallasite (Buseck 1977).

Dar al Gani (DaG) 978 is a type 3 ungrouped carbonaceous chondrite found in Libya in 1999 (Russell et al. 2003). Choe et al. (2010) briefly reported its petrography, mineralogy, bulk oxygen isotope compositions, and bulk chemistry. Zhang and Yurimoto (2013) reported the detailed petrographic and mineralogical features of this chondrite. They reveal that DaG 978 has experienced both thermal metamorphism and metasomatism, namely fluid-assisted metamorphism. Recently, we observed that some of the lath-shaped olivine grains in DaG 978 contain up to 5.5 wt% P_2O_5. In this study, we report the detailed texture and mineral chemistry of P-rich olivine in DaG 978, and discuss its formation mechanism and implications.

ANALYTICAL METHODS

In this study, we observe the petrographic textures of the olivine in DaG 978 by using a scanning electron microscope (SEM) at Purple Mountain Observatory (Hitachi S-3400N II) and a SEM at Nanjing University (JSM 6490), both located in Nanjing, China. Both of the two SEM instruments were operated at an accelerating voltage of 15 kV.

The mineral chemistry of olivine and its associated minerals was mainly determined by using an electron probe micro-analyzer (EPMA) at Nanjing University (JEOL 8100). The operating conditions were 15 kV accelerating voltage, 50 nA beam current, and a beam size of ~2 μm. The following natural and synthetic standards were used for quantitative analyses: fayalite for Si, Fe, and Mn; forsterite for Mg; fluorapatite for P; hornblende for Na, K, Al, Ca, and Ti; and Cr_2O_3 for Cr. Since fluorapatite contains volatile element F, which is sensitive to electron beams, P is the only element measured for the fluorapatite standard. A $Pb_5(PO_4)_3Cl$ standard was used as a secondary standard for P. Various peak-counting times were used for different elements; 10 s for Fe, Mg, Si, Na, and K; 60 s for Ca, Ti, Al, Mn, Cr; 150 s for P. Detection limits in olivine and pyroxene are: 20 ppm for CaO and P_2O_5; 30 ppm for Al_2O_3; 50 ppm for MnO and Cr_2O_3; 60 ppm for TiO_2 and Na_2O; 70 ppm for MgO; 90 ppm for SiO_2 and K_2O; and 180 ppm for FeO. All data were reduced with the ZAF procedure for the JEOL microprobe. The SEM X-ray elemental mapping was performed to reveal the distribution of P and other elements among different minerals. Mineral compositions for a few fine-grained minerals associated with P-rich olivine were determined by using a silicon-drift-detector (SDD) energy dispersive spectrometer (EDS) installed on a Zeiss Supra 55 Field-Emission-Gun (FEG) SEM at Nanjing University. The accelerating voltage is 10 kV. Instrument default standards were used for calculating the contents of major elements in the fine-grained minerals.

In order to study the micro-texture and chemical features of P-rich olivine and its associated minerals using transmission electron microscopy (TEM), we prepared a TEM foil of 7.3 × 1.7 μm in area by a focused ion beam (FIB) system. The FIB milling was conducted on a Zeiss Auriga Compact instrument at the Institute of Geology and Geophysics, Beijing. A layer of Pt was deposited over the region of interest to protect the surface from ion beam damage during sample preparation processes. After cutting, the TEM foil was lifted out from the bulk sample by using an Omniprobe AutoProbe200 micromanipulator and attached to a copper grid. Ion milling was carried out with an accelerating voltage of 30 kV and various beam currents. Final polishing of the thin foil was conducted with 4 kV. The TEM section is approximately 100 nm in thickness.

Textural observations and compositional analyses of P-rich olivine and its associated minerals were carried out using a FEI Tecnai F20 TEM instrument. This TEM instrument was accelerated at 200 kV for conventional bright field TEM observations, selected area electron diffraction (SAED), high angle annular dark field (HAADF) observations, and energy dispersive X-ray (EDX) analyses. The instrument default standards were used to calculate the Al/Cr values in Cr-rich hercynite. The latter two observations and analyses were conducted under scanning TEM mode. Elemental mapping under scanning TEM mode, which is controlled by an Oxford Aztec software, was performed to reveal the distribution of elements at given regions.

RESULTS

Olivine is widely present in amoeboid olivine aggregates (AOAs) and ferromagnesian chondrules from the DaG 978 chondrite. The olivine grains in AOA are fine-grained and always enclose Al-rich nodules or metal grains. They are Fe-rich (Mg#[≡Mg/(Mg+Fe) × 100] = 70–72), due to the Fe-Mg inter-diffusion (Zhang and Yurimoto 2013). They contain low concentrations of Al_2O_3 (0.005–0.061 wt%), Cr_2O_3 (0.026–0.044 wt%), TiO_2 (0.014–0.041 wt%), P_2O_5 (0–0.027 wt%), and CaO (0.018–0.097 wt%). In porphyritic olivine (PO) chondrules in DaG 978, olivine occurs as phenocrysts (>200 μm in size) and usually contain Mg-rich cores (Mg# = 100) and Fe-rich rims (Mg# = 69). In porphyritic olivine-pyroxene (POP) chondrules, olivine occurs as small, round-shaped grains (usually <100 μm in size) and is enclosed by low-Ca pyroxene. Most of these olivine grains are homogeneous in BSE images and have a limited chemical variation (Mg# = 69–75). The contents of Al_2O_3 (0.005–0.164 wt%), Cr_2O_3 (0.017–0.098 wt%), TiO_2 (0–0.153 wt%), P_2O_5 (0–0.017 wt%), and CaO (0.030–0.294 wt%) are generally low in these olivine grains.

Besides the primary olivine in AOAs and chondrules, lath-shaped olivine grains are also observed in DaG 978. The lath-shaped olivine occurs in different textures, surrounding round-shaped olivine, replacing enstatite, or forming aggregates (see Figs. 10d-e and Fig. 14 of Zhang and Yurimoto 2013). Some of these lath-shaped olivine grains contain fine-grained (<1 μm in width) nepheline inclusions (based on the EDS peaks of Na, K, Al, and Si; Zhang and Yurimoto 2013). The lath-shaped olivine grains

are Fe-rich with an Mg# value of 66–72, similar to those of fine-grained olivine in AOAs and chondrules. However, compared with the primary olivine in AOAs and chondrules, the lath-shaped olivine grains contain apparently higher contents of Al_2O_3 (0.018–1.097 wt%), Cr_2O_3 (0.036–0.909 wt%), TiO_2 (0–0.136 wt%), P_2O_5 (0–5.533 wt%), and CaO (0.022–0.763 wt%) (Fig. 1). The molar Cr/Al values generally range in ~1/2□1. Representative compositions of the P-rich olivine are given in Table 1, in comparison with the primary olivine in AOAs and chondrules. The P_2O_5 concentrations of these olivine grains exhibit a negative correlation with the SiO_2 concentrations (Fig. 2). It is noteworthy that olivine grains with high P_2O_5 contents (>1 wt%) usually contain low cation totals (Table 1). Although most of the lath-shaped olivine grains in DaG 978 generally contain P_2O_5 higher than those in primary olivine (Fig. 1), P-rich olivine (P_2O_5>1 wt%) is not widely present in DaG 978 and only observed in a ferromagnesian chondrule (named as PC-1) and an adjacent mineral fragment (Figs. 3–4). The the PC-1 chondrule mainly consists of round-shaped olivine, low-Ca pyroxene ($En_{83}Fs_{14}Wo_3$ with 1.05 wt% Al_2O_3 and 0.38 wt% Cr_2O_3 based on EPMA data, Cr/Al ~1/4), and Na-rich plagioclase ($Ab_{71}An_{29}$ based on SEM-EDS data). Minor minerals in PC-1 are FeNi metal, troilite, Cr-rich hercynite (Cr/Al ~1 based on SEM-EDS data), chlorapatite, and merrillite (Fig. 3b). The P-rich olivine mainly occurs at the margin of the PC-1 chondrule (Figs. 3b–d) and contains up to 2.7 wt% P_2O_5. In PC-1, the P-rich olivine (<10 μm in size) can be distinguished from the primary olivine, based on their textural difference and whether they contain bright inclusions (Figs. 3b-d). The primary olivine occurs as “clean” and

round-shaped grains in BSE images and contains no bright inclusions, whereas the P-rich olivine are "dusty" with many tiny bright inclusions and seldom occurs as round-shaped grains. The P-rich olivine has a lath-like shape, although it is not as typical as those described in Zhang and Yurimoto (2013). The P-rich olivine grains enclose primary olivine grains and partially replace low-Ca pyroxene grains. One olivine grain adjacent to PC-1 is also P-rich (Fig. 3a), and is the only olivine grain with up to ~5 wt% P_2O_5. This grain is probably a remnant of an originally larger fragment (named as PF-1) shown in Fig. 4. However, unfortunately, most part of the original fragment (PF-1) was lost during repolishing the thin section after other measurements. X-ray elemental mapping results before repolishing reveal that a P-rich rim encloses a P-poor core, which apparently contains three olivine grains. The boundary between the P-rich rim and the P-poor core is sharp in both the BSE image and elemental X-ray maps. Phosphorus distributes heterogeneously but continuously in the rim (Fig. 4e). However, Cr and Al disperse in the P-rich rim as hot spots (Figs. 4g-h), corresponding to the tiny bright inclusions in the rim (Fig. 4a).

A FIB-TEM foil was cut from a region of P-rich olivine in the PC-1 chondrule (Fig. 3c). This foil is composed dominantly of olivine, with minor plagioclase (Fig. 5). Both P-rich olivine and plagioclase contain fine-grained Cr-rich hercynite inclusions (20–160 nm in size; Figs. 5–6). Chlorapatite and merrillite are also detected based on the X-ray mapping results for P, Ca, and Cl (Figs. 7–8). Our EDS analyses under the STEM mode

reveal that some of the olivine grains have a high peak for P while some of the olivine grains do not have the peak for P (Fig. 6). The heterogeneous distribution of P in olivine is also supported by the mapping result of P for the olivine grains (Fig. 8). This is consistent with the SEM-EDS mapping result on the P-rich olivine grain shown in Fig. 4. It is noteworthy that the olivine grains containing Cr-rich hercynite inclusions have no visible peaks for Cr and Al (Fig. 6). The TEM-EDS analyses show that the Cr-rich hercynite grains have a molar Cr/Al value of ~1/2. Additionally, no large chemical variation can be observed for the Cr-rich hercynite grains associated with P-rich olivine and plagioclase, respectively (Fig. 7).

DISCUSSION

Chemical features of P-rich olivine in DaG 978

Phosphorus-rich olivine is a relatively uncommon phase in both terrestrial and extraterrestrial materials. In this study, the TEM observations indicate that the P-rich olivine is closely associated with fine-grained Ca-phosphate minerals. Therefore, we reduced the P_2O_5 contents by assuming that all CaO and some P_2O_5 in EPMA data for P-rich olivine are due to contamination from merrillite (Table 1). The reduced results are comparable with the apparent P_2O_5 contents (Table 1), indicating that the high P_2O_5 contents in olivine are not due to contamination from Ca-phosphate minerals. This conclusion is well consistent with the qualitative characterization with the TEM-EDS

213 method (Fig. 6). Therefore, the P-rich olivine in DaG 978 represents its new occurrence
214 in nature, rather than a result of contamination from Ca-phosphate minerals.

215 The negative correlation between P and Si in P-rich olivine demonstrates that P
216 incorporates into the crystal structure of olivine by substituting Si, as suggested by all
217 previous investigations (Buseck 1977; Buseck and Clark 1984; Goodrich 1984; Agrell et
218 al. 1998; Wasson 1999; Tropper et al. 2004; Wang et al. 2007; Sonzogni et al. 2009;
219 Boesenberg and Hewins 2010; Schneider et al. 2013; Fowler-Gerace and Tait 2015). Our
220 EPMA results show that P-rich olivine in DaG 978 contains much higher apparent Cr_2O_3
221 and Al_2O_3 values than those in AOAs and chondrules. However, the TEM observations
222 and analyses indicate that the Cr and Al concentrations in P-rich olivine from DaG 978
223 are very low, probably on the same level of olivine in AOAs and chondrules. The
224 apparently high Cr and Al concentrations in P-rich olivine should be due to
225 contaminations from the tiny Cr-rich hercynite inclusions. Therefore, we suggest that the
226 incorporation of P in olivine from DaG 978 is not related to Cr and Al (Milman-Barris et
227 al. 2008; McCanta et al. 2016). Instead, all the P-rich olivine grains in DaG 978 contain
228 low cation totals based on 4 oxygen atoms (Table 1), indicating the presence of cation
229 vacancy. Generally, olivine with higher P_2O_5 contents contains higher cation vacancies,
230 based on the data for lath-shaped olivine shown in Table 1. This implies that the
231 incorporation of P into olivine crystal structure should be related to the presence of cation
232 vacancy. Therefore, P might incorporate into the crystal structure of olivine through the

233 substitution $2^{IV}Si^{4+} + 4^{VI}M^{2+} \Leftrightarrow 2^{IV}P^{5+} + 3^{VI}M^{2+} + {}^{VI}[]$, as proposed by Boesenberg and
234 Hewins (2010) based on synthetic experimental P-rich olivine.

235 **Formation mechanism of P-rich olivine in DaG 978**

236 Formation mechanism of P-rich olivine has been discussed in previous
237 investigations on natural and synthetic samples (Goodrich 1984; Agrell et al. 1998;
238 Tropper et al. 2004; Wang et al. 2007; Boesenberg and Hewins 2010; Schneider et al.
239 2013; Fowler-Gerace and Tait 2015). Most of these investigations suggested that rapid
240 crystallization from a high-temperature (>~1000 °C) P-rich melt is the most viable
241 mechanism for the formation of P-rich olivine (see Boesenberg and Hewins 2010;
242 Fowler-Gerace and Tait 2015). The scenario is well supported by the igneous texture of
243 the samples containing P-rich olivine or the internal texture of P-rich olivine, although
244 the host samples of P-rich olivine have different mineral assemblages and origins.
245 However, this scenario cannot interpret the origin of P-rich olivine in DaG 978, since the
246 P-rich olivine and its associated minerals do not exhibit an igneous texture. A new
247 mechanism is required to interpret the formation of this P-rich olivine.

248 Zhang and Yurimoto (2013) described that olivine in AOAs and normal chondrules
249 from DaG 978 has much lower Mg# values than its associated pyroxene. This feature is
250 also observed in this study for the olivine and pyroxene in PC-1. This chemical feature
251 has been interpreted as a result of various Fe-Mg interdiffusion rates in olivine and
252 pyroxene during a metamorphic event on the parent body (Zhang and Yurimoto 2013;

Zhang et al. 2014). Although the P-rich olivine in DaG 978 has Mg# values similar to those in AOAs and chondrules, it is unlikely that the elevated P_2O_5 concentrations in olivine are due to elemental diffusion during the metamorphic event. If the high P_2O_5 concentrations in lath-like olivine grains were due to thermal metamorphism, some, if not all, of the olivine grains in AOAs and normal chondrules would be enriched in phosphorus as well. However, this is not observed in this study. P-rich olivine shows a sharp boundary with P-poor olivine (Fig. 4e). The absence of P-enrichment in olivine from AOAs and normal chondrules is consistent with the low diffusion of P in olivine (Milman-Barris et al. 2008; Watson et al. 2015; McCanta et al. 2016).

The lath-shaped texture and chemical feature indicates that the P-rich olivine could have formed during fluid-assisted metamorphism on the DaG 978 parent body. Fluid-assisted metamorphism is a kind of metamorphism in the presence of fluids (Krot et al. 2004; Brearley and Krot 2013). It involves both metamorphism and metasomatism, and has been widely accepted as the formation mechanism of the secondary ferrous olivine in many carbonaceous chondrites (e.g., Krot et al. 2004; Brearley and Krot 2013; Zhang and Yurimoto 2013). Fluid-assisted metamorphism has been proposed to interpret other secondary mineralogical and oxygen isotopic features in DaG 978 (Zhang and Yurimoto 2013; Zhang et al. 2014), which supports our interpretation about the formation of P-rich olivine.

Based on petrographic observations and the isotopic compositions of ferrous olivine,

Krot et al. (2004) proposed three different formation mechanism of secondary ferrous olivine during fluid-assisted metamorphism: (i) replacement of FeNi-metal ± sulfide nodules, (ii) replacement of magnesian olivine and low-Ca pyroxene, and (iii) direct precipitation from an aqueous solution. Here, we will discuss the formation mechanism of P-rich olivine based on our observations on the chondrule PC-1. The presence of FeNi metal and troilite as intact grains in PC-1 indicates that the formation of P-rich olivine is not due to replacement of FeNi-metal ± sulfide nodules. Instead, it could have formed through replacing olivine and/or enstatite, since petrographic observations demonstrate that P-rich olivine encloses round-shaped olivine and irregular enstatite grains. Given that low-Ca pyroxene contains higher Cr and Al concentrations than the primary olivine in DaG 978 (Zhang and Yurimoto 2013; this study), the presence of tiny Cr-rich hercynite inclusions indicates that P-rich olivine probably has formed through replacing enstatite rather than primary olivine (c.f., Brearley and Krot 2013). The Cr and Al in Cr-rich hercynite might be derived from the precursor low-Ca pyroxene. With low mobility of Cr in aqueous solution (Roeder and Reynolds 1991; Klein-BenDavid et al. 2001), Cr-rich hercynite could have precipitated during the formation of P-rich olivine. We noticed that the Cr/Al ratios (~1/2□1) of the fine-grained Cr-rich hercynite are generally comparable with those of P-rich olivine (1/2□1), but higher than that of low-Ca pyroxene (1/8□1/3; Zhang and Yurimoto 2013; this study). This discrepancy could be due to the presence of secondary plagioclase (Fig. 5) and/or due to the loss of Al into fluids, since the replacement process should have taken place in an open system. In addition, the shape of

294 enstatite and olivine in the chondrule fragment shown in Fig. 3 also supports that enstatite
295 could be the precursor mineral, although it might not be definitive evidence. The
296 coexistence of Cr-rich hercynite with P-rich olivine and the replacement texture can also
297 exclude the possibility that P-rich olivine formed through direct precipitation from
298 aqueous solution. The first and key consideration is that direct precipitation of Cr-rich
299 hercynite and P-rich olivine cannot account for the replacement texture of low-Ca
300 pyroxene. The second consideration is the low solubility and high immobility of Cr^{3+} in
301 aqueous solution (e.g., Roeder and Reynolds 1991; Klein-BenDavid et al. 2011),
302 although Watenphul et al. (2014) reported elevated Cr^{3+} solubility in aqueous fluids at
303 high pressures and temperatures. In summary, it is most likely that the Cr in hercynite is
304 derived from the precursor low-Ca pyroxene rather than the aqueous solution. The P-rich
305 olivine in DaG 978 could have formed by replacing precursor low-Ca pyroxene during
306 fluid-assisted metamorphism.

307 **Formation conditions of P-rich olivine in DaG 978**

308 Although P-rich olivine in DaG 978 should have formed through a mechanism
309 differing from other natural P-rich olivine described in the literature, there are two
310 aspects of similarities for their formations. First, the system from which P-rich olivine
311 crystallized should have high P_2O_5 concentrations and low silica activity (Goodrich 1984;
312 Agrell et al. 1998; Boesenberg and Hewins 2010; Schneider et al. 2013; Fowler-Gerace
313 and Tait 2015). This chemical requirement that has been extensively emphasized in the

literature is also supported by the petrographic observations in DaG 978. In DaG 978, the TEM observations reveal that P-rich olivine shows a spatially close association with chlorapatite and merrillite, which indicates a high P_2O_5 concentration. Meanwhile, the replacement of low-Ca pyroxene by olivine is consistent with a low silica activity.

Second, the texture of other natural P-rich olivine demonstrates a rapid crystallization from high-temperature melts (Goodrich 1984; Tropper et al. 2004; Schneider et al. 2013; Fowler-Gerace and Tait 2015). Previous investigations suggest that P-rich olivine should be a metastable phase during a disequilibrium process. This is well consistent with the synthetic experimental results by Boesenberg and Hewins (2010), in which the P_2O_5 contents in olivine decrease with duration. For the P-rich olivine in DaG 978, it should also be a product of disequilibrium process, although its crystallization kinetics remains unknown. The main evidence for such a disequilibrium process is the heterogeneous distribution of P among secondary olivine grains and even within single grains (Figs. 4 and 8).

Differing from other natural P-rich olivine that could have formed under high temperature (>1000 °C; Boesenberg and Hewins 2010; Fowler-Gerace and Tait 2015), however, the P-rich olivine in DaG 978 should have formed under a relatively lower temperature. The absence of phyllosilicate minerals and the petrologic type of DaG 978 indicate that the formation temperature of P-rich olivine might be as low as 400–650 °C or even lower (Jones and Rubie 1993; Zhang and Yurimoto 2013). It is difficult to

interpret the stability of P-rich olivine with the phase diagram between forsterite and farringtonite [$Mg_3(PO_4)_2$], because forsterite and farringtonite cannot form a solid solution at an equilibrium temperature below 1320 °C (Boesenberg and Hewins 2010). For the case of the P-rich olivine in DaG 978, we suspect that its formation might be related to two reasons. One is the disequilibrium formation process as discussed above. The other could be the high FeO contents of the P-rich olivine (~Fa_{30}) in DaG 978. Compared with Fe-poor olivine, Fe-rich olivine usually forms at a lower temperature. Although whether and how Fe^{2+} affects the solubility of P in olivine remains unknown, most P-rich olivine grains in natural samples and experimental products contain high FeO contents (Boesenberg and Hewins 2010).

The P-rich fluid has been proposed in our previous investigations on the DaG 978 chondrite (Zhang and Yurimoto 2013; Zhang et al. 2016), which contains much more abundant coarse-grained chlorapatite than other type 3 chondrites to our knowledge. Based on the close association between apatite and merrillite and FeNi metal, it is very likely that FeNi metal could be one of the most important sources of P (Zanda et al. 1994; Zhang et al. 2016). In addition, mesostasis could be another source of P. Jones (1990) reported that the mesostasis in type II chondrules could contain up to 3.5 wt% P_2O_5. As for the chondrule PC-1 and the adjacent P-rich olivine fragment PF-1, it is difficult to constrain the source of P. However, based on small amount of FeNi metal in PC-1, an external source of P might be more likely to interpret the presence of chlorapatite,

merrillite, and P-rich olivine. As for the local occurrence of P-rich olivine in DaG 978, we suspect that it could be related to local chemistry (e.g., P and Ca) of fluids and the minerals that have been replaced or altered. If the fluid has high activities for both P and Ca, Ca-phosphate minerals would be the dominant P-rich phases and suppress the formation of P-rich olivine. However, if the fluid has a high P activity but a low activity of Ca, some P might incorporate into the olivine structure while Ca-phosphate minerals are also precipitates from the fluid. Laboratory experiments are needed to confirm this scenario.

IMPLICATIONS

Phosphorus-rich olivine was considered as an anomalous phase compared with the normal olivine in igneous samples of terrestrial and extraterrestrial origins. It was suggested that P-rich olivine formed through rapid crystallization from high-temperature P-rich melts. Although this scenario was not explicitly claimed as the only mechanism forming P-rich olivine, it was considered as the most viable mechanism (Boesenberg and Hewins 2010; Fowler-Gerace and Tait 2015). Our study described a new occurrence of natural P-rich olivine and demonstrates a new formation mechanism involving replacement of low-Ca pyroxene by P-rich fluids during fluid-assisted metamorphism. The most distinctive difference between our interpretation and that in the literature is the formation temperature. Such a comparison implies that high temperature is not a key factor affecting the solubility of P in olivine. Instead, high P concentration and

374 disequilibrium formation process could be the two predominant factors for the formation
375 of P-rich olivine.

376 We noticed that not all of the P-rich olivine grains reported in the literature have a
377 texture explicitly indicating a rapid crystallization from high-temperature melts (Agrell et
378 al. 1998; Wang et al. 2007). Therefore, rapid crystallization from high-temperature melts
379 might not be the only interpretation for these two occurrences of P-rich olivine. Instead,
380 fluid-assisted metamorphism might be an alternative interpretation. First, for the case of
381 P-rich olivine from Pine Canyon, Piute Co., Utah (Agrell et al. 1998), the sample did not
382 exhibit a dendritic texture as other terrestrial occurrences of P-rich olivine. On the other
383 hand, the authors stated that the samples resemble the olivine-rich group of the highly
384 desilicated 'skarns' (Agrell et al. 1998). This seems to be similar to the replacement of
385 low-Ca pyroxene by olivine in DaG 978, which can also considered as a means of
386 desilication. Second, for the case of P-rich olivine in the Ningqiang carbonaceous
387 chondrite, it is closely associated with opaque assemblages (Fig. 2b of Wang et al. 2007).
388 The opaque assemblages in the Ningqiang chondrite contain magnetite, phosphate
389 minerals, pyrrhotite, and relict primary minerals (Hsu et al. 2006). Hsu et al. (2006)
390 suggested that the magnetite and phosphate minerals in opaque assemblages from the
391 Ningqiang chondrite should have formed by aqueous alteration, based on their oxygen
392 isotopic compositions. Considering the spatially close association between P-rich olivine
393 and magnetite and phosphate minerals, it is very likely that the P-rich olivine also formed

by metasomatism of preexisting metal alloys during fluid-assisted metamorphism. If these interpretations are correct, formation of P-rich olivine through fluid-assisted metamorphism would also be common. However, we cannot completely rule out the possibility that the P-rich olivine in these two occurrences has a high-temperature crystallization origin.

ACKNOWLEDGEMENTS

This study is financially supported by Natural Science Foundation of China (Grant no. 41373065) and the Fundamental Research Funds for the Central Universities. We thank Run-Lian Pang for helpful discussions. We appreciate the comments from Dr. Kimberly Tait and Dr. John Beckett and the editorial effort from Associate Editor Prof. E. Watson.

REFERENCES CITED

Agrell, S.O., Charnley, N.R., and Chinner, G.A. (1998) Phosphoran olivine from Pine Canyon, Piute Co., Utah. Mineralogical Magazine, 62, 265–269.

Anderson, A.T., and Greenland, L.P. (1969) Phosphorus fractionation diagram as a quantitative indicator of crystallization differentiation of basaltic liquids. Geochimica et Cosmochimica Acta, 33, 493–505.

Boesenberg, J.S., and Hewins, R.H. (2010) An experimental investigation into the metastable formation of phosphoran olivine and pyroxene. Geochimica et

413 Cosmochimica Acta, 74, 1923–1941.

414 Brearley, A.J. and Krot, A.N. (2013) Metasomatism in the early solar system: the record
415 from chondritic meteorites. In Metasomatism and the chemical transformation of
416 rock, Lecture notes in Earth System Sciences, edited by Harlov D. E. and Austrheim
417 H. Berlin: Springer-Verlag. pp. 659–789.

418 Brunet, F., and Chazot, G. (2001) Partitioning of phosphorus between olivine,
419 clinopyroxene and silicate glass in a spinel lherzolite xenolith from Yemen.
420 Chemical Geology, 176, 51–72.

421 Buseck, P.R. (1977) Pallasite meteorites—Mineralogy, petrology and geochemistry.
422 Geochimica et Cosmochimica Acta, 41, 711–740.

423 Buseck, P.R., and Clark, J. (1984) Zaisho—A pallasite containing pyroxene and
424 phosphoran olivine. Mineralogical Magazine, 48, 229–235.

425 Choe, W.H., Huber, H., Rubin, A.E., Kallemeyn, G.W., and Wasson, J.T. (2010)
426 Compositions and taxonomy of 15 unusual carbonaceous chondrites. Meteoritics &
427 Planetary Science, 45, 531–554.

428 Fowler-Gerace, N.A., and Tait, K.T. (2015) Phosphoran olivine overgrowth: Implications
429 for multiple impacts to the Main Group pallasite parent body. American
430 Mineralogist, 100, 2043–2052.

431 Goodrich, C.A. (1984) Phosphoran pyroxene and olivine in silicate inclusions in natural
432 iron-carbon alloy, Disko Island, Greenland. Geochimica et Cosmochimica Acta, 48,

2769–2771.

Grossman, J.N., and Brearley, A.J. (2005) The onset of metamorphism in ordinary and carbonaceous chondrites. Meteoritics & Planetary Science, 40, 87–122.

Hsu, W., Guan, Y., Hua, X., Wang, Y., Leshin, L.A., and Sharp, T.G. (2006) Aqueous alteration of opaque assemblages in the Ningqiang carbonaceous chondrite: Evidence from oxygen isotopes. Earth and Planetary Science Letters, 243, 107–144.

Jones, R.H. (1990) Petrology and mineralogy of type II, FeO-rich chondrules in Semarkona (LL3.0): Origin by closed-system fractional crystallization, with evidence for supercooling. Geochimica et Cosmochimica Acta, 54, 1785–1802.

Jones, R.H., and Rubie, D.C. (1993) Thermal histories of CO3 chondrites: application of olivine diffusion modelling to parent body metamorphism. Earth and Planetary Science Letters, 106, 73–86.

Klein-BenDavid, O., Pettke, T., and Kessel, R. (2011) Chromium mobility in hydrous fluids at upper mantle conditions. Lithos, 125, 122–130.

Krot, A.N., Petaev, M.I., and Bland, P.A. (2004) Multiple formation mechanisms of ferrous olivine in CV3 carbonaceous chondrites during fluid-assisted metamorphism. Antarctic Meteorite Research, 17, 154–172.

McCanta, M.C., Beckett, J.R., and Stolper, E.M. (2016) Correlations and zoning patterns of phosphorus and chromium in olivine from H chondrites and the LL chondrite Semarkona. Meteoritics & Planetary Science, 51, 520–546.

453 Milman-Barris, M.S., Beckett, J.R., Baker, M.B., Hofmann, A.E., Morgan, Z., Crowley,
454 M.R., Vielzeuf, D., and Stolper, E. (2008) Zoning of phosphorus in igneous olivine.
455 Contributions to Mineralogy and Petrology, 155:739–765.

456 Roeder. P.L., and Reynolds, I. (1991) Crystallization of chromite and chromium
457 solubility in basaltic melts. Journal of Petrology, 32, 909–934.

458 Russell, S.S., Zipfel, J., Folco, L., Jones, R., Grady, M.M., McCoy, T., and Grossman, J.
459 N. (2003) The Meteoritical Bulletin, No. 87. Meteoritics & Planetary Science, 38,
460 A189–A248.

461 Schneider, P., Tropper, P., and Kaindl, R. (2013) The formation of phosphoran olivine
462 and stanfieldite from the pyrometamorphic breakdown of apatite in slags from a
463 prehistoric ritual immolation site (Goldbichl, Igls, Tyrol, Austria). Mineralogy and
464 Petrology, 107, 327–340.

465 Sonzogni, Y., Devouard, B., Provost, A., and Devidal, J.-L. (2009) Olivine-hosted melt
466 inclusions in the Brahin pallasite. In Meteoritics and Planetary Science Supplement,
467 p. 5070, 72nd Annual Meeting of the Meteoritical Society, Nancy, France.

468 Tropper, P., Recheis, A., and Konzett, J. (2004) Pyrometamorphic formation of
469 phosphorus-rich olivines in partially molten metapelitic gneisses from a prehistoric
470 sacrificial burning site (Ötz Valley, Tyrol, Austria). European Journal of Mineralogy,
471 16, 631–640.

472 Wang, Y., Hua, X., and Hsu, W. (2007) Petrogenesis of opaque assemblages in the

473 Ningqiang carbonaceous chondrite. Science in China Series D: Earth Sciences, 50,
474 886–896.

475 Wasson, J.T., Lange, D.E., and Francis, C.A. (1999) Massive chromite in the Brenham
476 pallasite and the fractionation of Cr during the crystallization of asteroidal cores.
477 Geochimica et Cosmochimica Acta, 63, 1219–1232.

478 Watenphul, A., Schmidt, C., and Jahn, S. (2014) Cr(III) solubility in aqueous fluids at
479 high pressures and temperatures. Geochimica et Cosmochimica Acta, 126, 212–227.

480 Watson, E.B., Cherniak, D.J., and Holycross, M.E. (2015) Diffusion of phosphorus in
481 olivine and molten basalt. American Mineralogist, 100, 2053–2065.

482 Zanda, B., Bourot-Denise, M., Perron, C., and Hewins, R.H. (1994) Origin and
483 metamorphic redistribution of silicon, chromium, and phosphorus in the metal of
484 chondrites. Science, 265, 1846–1849.

485 Zhang, A.C., and Yurimoto, H. (2013) Petrography and mineralogy of the ungrouped type
486 3 carbonaceous chondrite Dar al Gani 978. Meteoritics & Planetary Science, 48,
487 1651–1677.

488 Zhang, A.C., Itoh, S., Sakamoto, N., Wang, R.C., and Yurimoto, H. (2014) Origins of
489 Al-rich chondrules: Clues from a compound Al-rich chondrule in the Dar al Gani
490 978 carbonaceous chondrite. Geochimica et Cosmochimica Acta, 130, 78–92.

491 Zhang, A.C., Li, Q.L., Yurimoto, H., Sakamoto, N., Li, X.H., Hu, S., Lin, Y.T., and Wang,

492 R.C. (2016) Young asteroidal fluid activity revealed by absolute age from apatite in
493 carbonaceous chondrite. Nature Communications, 7, 12844 doi:
494 10.1038/ncomms12844.

495 ## FIGURE CAPTIONS

496 **Figure 1**. Histogram of P_2O_5, Al_2O_3, and Cr_2O_3 contents (wt%) of olivine in AOAs, type
497 I chondrules, and lath-shaped grains.

498 **Figure 2**. Si (apfu) *versus* P (apfu) of lath-shaped olivine in DaG 978 and the data in the
499 literature (Buseck 1977; Goodrich 1984; Buseck and Clark 1984; Agrell 1998; Tropper
500 2004; Wang et al. 2007; Schneider et al. 2013; Fowler-Gerace and Tait 2015). apfu: atoms
501 per formula unit (on the basis of 4 oxygen atoms). The low Si values for P-poor olivine in
502 DaG 978 are due to the presence of Al and Cr.

503 **Figure 3**. (a) Backscattered electron (BSE) image of a ferromagnesian chondrule
504 fragment in DaG 978. (b-d) magnified images of the chondrule fragment. The chondrule
505 fragment mainly consists of P-poor olivine which exhibits a round shape, low-Ca
506 pyroxene, and Na-rich plagioclase. Minor minerals in this chondrule fragment are FeNi
507 metal, troilite, Cr-hercynite, chlorapatite, and merrillite. The P-rich olivine mainly occurs
508 at the margin of this chondrule fragment, replacing low-Ca pyroxene and containing tiny
509 bright inclusions. The location of FIB-TEM foil is signed in the (c).

510 **Figure 4**. (a) BSE image of a zoned olivine fragment adjacent to the chondrule fragment
511 shown in Fig. 3a. (b-h) X-ray mapping results of Si, Mg, Fe, P, Ca, Cr, Al. Note that P
512 distributes continuously, but heterogeneously in the rim of the olivine fragment whereas
513 Cr and Al hot spots disperse in the P-rich rim.

514 **Figure 5**. HAADF image of the P-rich olivine. It is associated with a plagioclase grain.

Both the P-rich olivine and the plagioclase grains contain Cr-hercynite grains (the small bright grains) as inclusions. The two square regions are mapped to show the elemental distributions (Fig. 7 and Fig. 8).

Figure 6. TEM-EDS spectra of P-rich olivine (a), P-poor olivine (b), and Cr-rich hercynite (c) in the FIB-TEM foil shown in Fig. 5.

Figure 7. (a) HAADF image of P-rich olivine and plagioclase. (b-i) STEM-EDS mapping results of Si, Mg, Fe, Al, Cr, P, Ca, and Cl. The high intensities of Fe, Al, and Cr indicate that the bright grains in (a) are Cr-rich hercynite. The distributions of P, Ca, and Cl indicate that both apatite and merrillite are present in the analyzed region. Note that olivine contains higher P concentrations than plagioclase.

Figure 8. (a) HAADF image of P-rich olivine and its Cr-rich hercynite inclusions. (b-i) EDS mapping results of Si, Mg, Fe, Al, Cr, P, Ca, and Cl. The high intensities of Fe, Al, and Cr indicate that the bright grains in (a) are Cr-rich hercynite. The distributions of P, Ca, and Cl indicate that apatite is present in the analyzed region. Note that P distributes heterogeneous in the analyzed region (g).

530 Table 1. Representative EPMA compositions of olivine in DaG 978

	AOA		Chondrules		Lath-shaped olivine						
P_2O_5	0.01	bdl	bdl	bdl	5.53	2.71	1.97	1.60	1.54	0.13	0.05
P_2O_5*	bdl	bdl	bdl	bdl	5.27	2.56	1.82	0.88	0.79	0.09	0.03
SiO_2	37.3	37.8	37.5	36.8	31.9	33.8	34.7	35.2	35.2	37.2	36.8
TiO_2	0.02	0.03	0.07	0.09	0.04	0.08	0.07	0.14	0.09	0.03	0.02
Al_2O_3	0.02	0.02	0.05	0.04	1.10	0.82	0.58	0.93	1.10	0.71	0.50
Cr_2O_3	0.04	0.03	0.09	0.04	0.84	0.91	0.66	0.68	0.89	0.63	0.22
FeO	25.5	26.9	28.2	27.8	27.9	28.4	27.6	28.1	27.5	25.3	28.0
MnO	0.31	0.27	0.27	0.28	0.24	0.23	0.22	0.25	0.22	0.17	0.20
MgO	36.2	35.9	34.2	35.5	31.0	31.1	33.0	31.7	31.6	36.6	34.9
CaO	0.02	0.05	0.07	0.06	0.26	0.15	0.15	0.73	0.76	0.04	0.02
Na_2O	0.01	bdl	0.01	bdl	0.27	0.07	0.04	0.07	0.05	bdl	bdl
K_2O	bdl	0.01	0.01	0.01	0.01	0.01	bdl	bdl	bdl	bdl	bdl
Total	99.43	101.0	100.5	100.6	99.09	98.28	98.99	99.40	98.95	100.8	100.7
Calculated based on 4 oxygen atoms											
P	0.000	bdl	bdl	bdl	0.126	0.062	0.045	0.036	0.035	0.003	0.001
Si	0.990	0.993	0.998	0.978	0.856	0.922	0.935	0.948	0.951	0.973	0.976
Ti	0.000	0.001	0.001	0.002	0.001	0.002	0.001	0.003	0.002	0.001	0.000
Al	0.001	0.001	0.001	0.001	0.035	0.026	0.019	0.029	0.035	0.022	0.016
Cr	0.001	0.001	0.002	0.001	0.018	0.020	0.014	0.014	0.019	0.013	0.005
Fe	0.565	0.588	0.625	0.614	0.625	0.645	0.620	0.631	0.618	0.551	0.619
Mn	0.007	0.006	0.006	0.006	0.005	0.005	0.005	0.006	0.005	0.004	0.004
Mg	1.443	1.416	1.364	1.415	1.250	1.272	1.335	1.282	1.280	1.437	1.390
Ca	0.001	0.001	0.002	0.002	0.007	0.004	0.004	0.021	0.022	0.001	0.001
Na	0.001	bdl	0.000	bdl	0.014	0.004	0.002	0.004	0.003	bdl	bdl
K	bdl	0.000	0.000	0.000	0.000	0.000	bdl	bdl	bdl	bdl	bd
Sum	3.009	3.006	3.000	3.019	2.936	2.962	2.981	2.974	2.970	3.004	3.012
Mg#	72	71	69	70	67	66	68	67	67	72	69

531 Bdl: below detection limit; Mg# = Mg/(Mg+Fe)×100 in mole.

532 P_2O_5*=P_2O_5□CaO×47.32/48.08, based on the assumption that merrillite contributes all
533 the CaO contents.

534

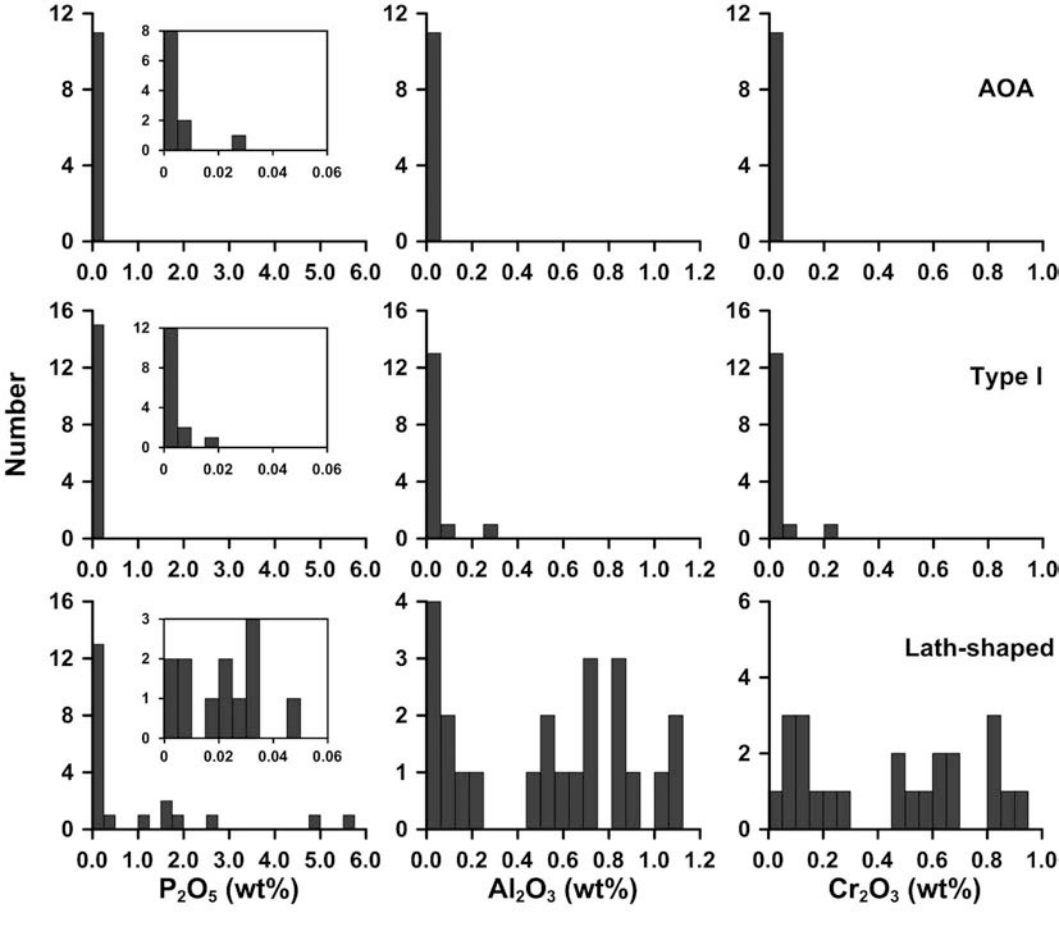

Figure 1

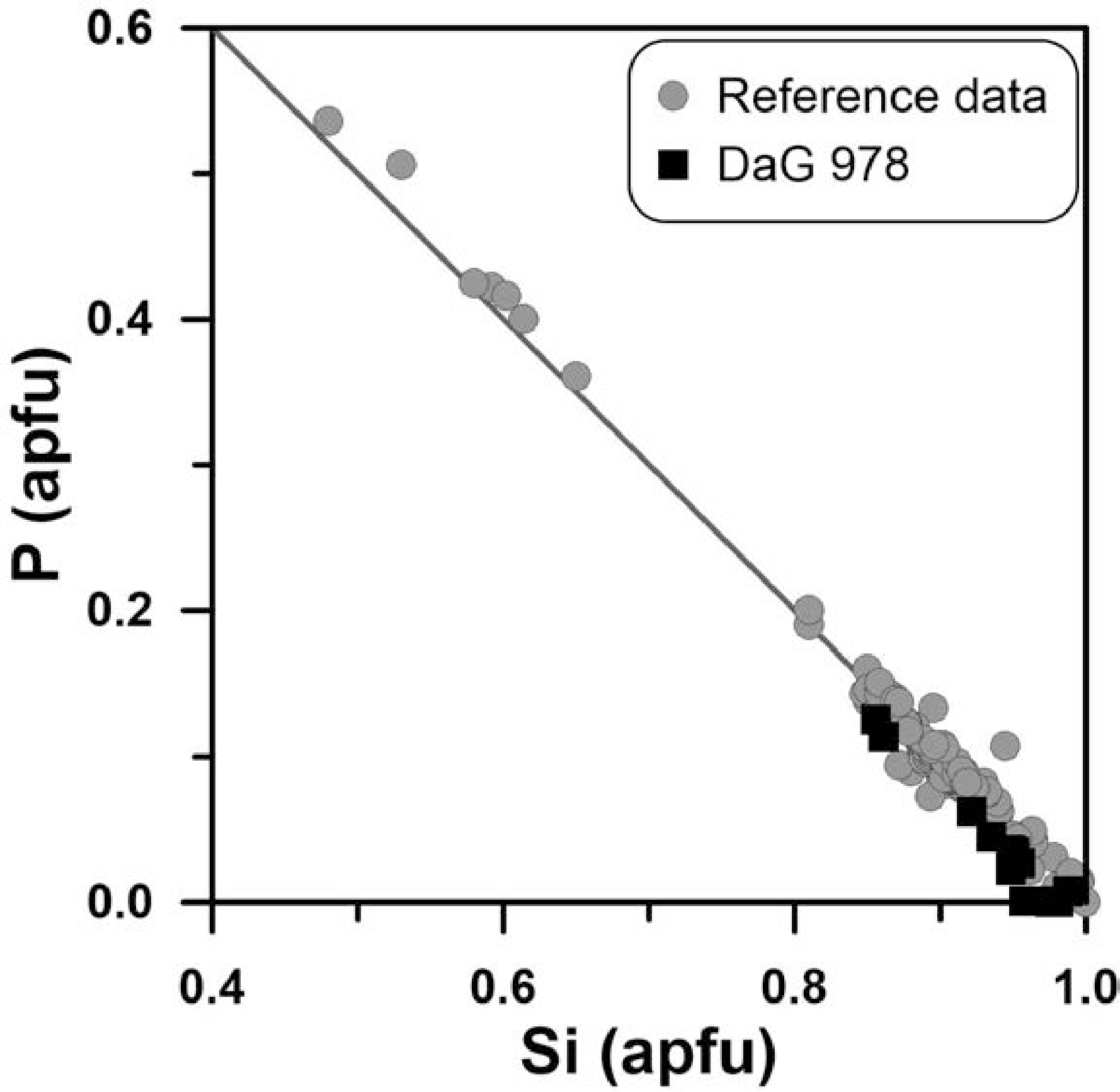

Figure 2

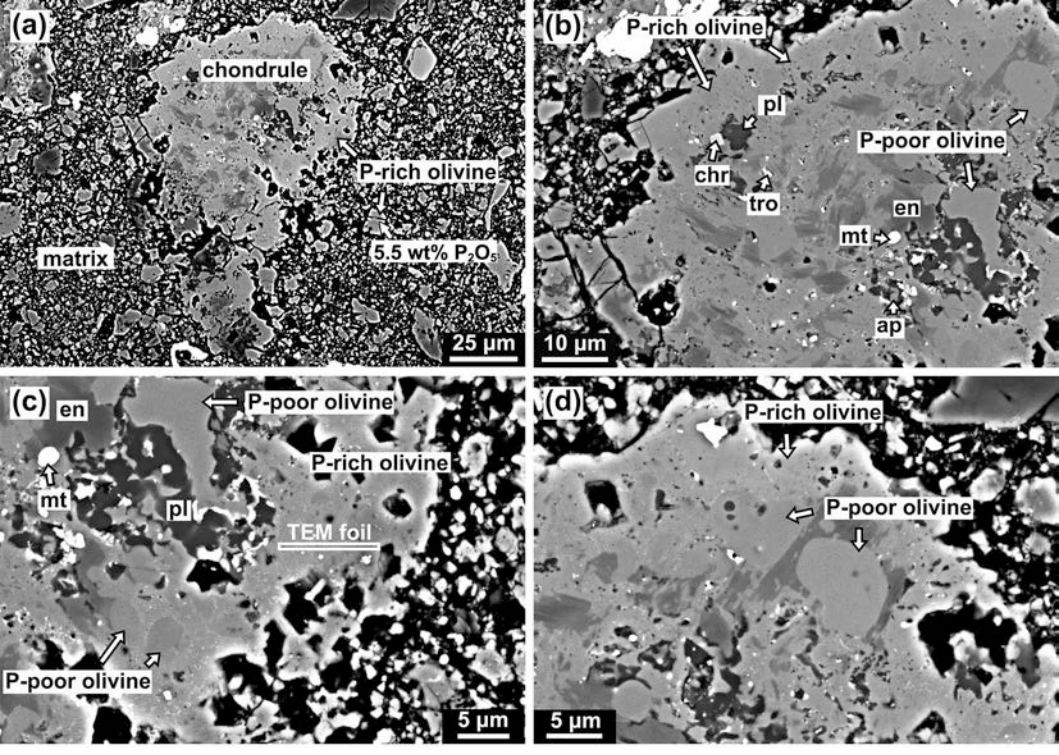
(a)
chondrule
P-rich olivine
matrix
5.5 wt% P_2O_5
25 μm
(b)
P-rich olivine
pl
P-poor olivine
chr
tro
en
mt
ap
10 μm
(c)
en
P-poor olivine
P-rich olivine
mt
pl
TEM foil
P-poor olivine
5 μm
(d)
P-rich olivine
P-poor olivine
5 μm

Figure 3

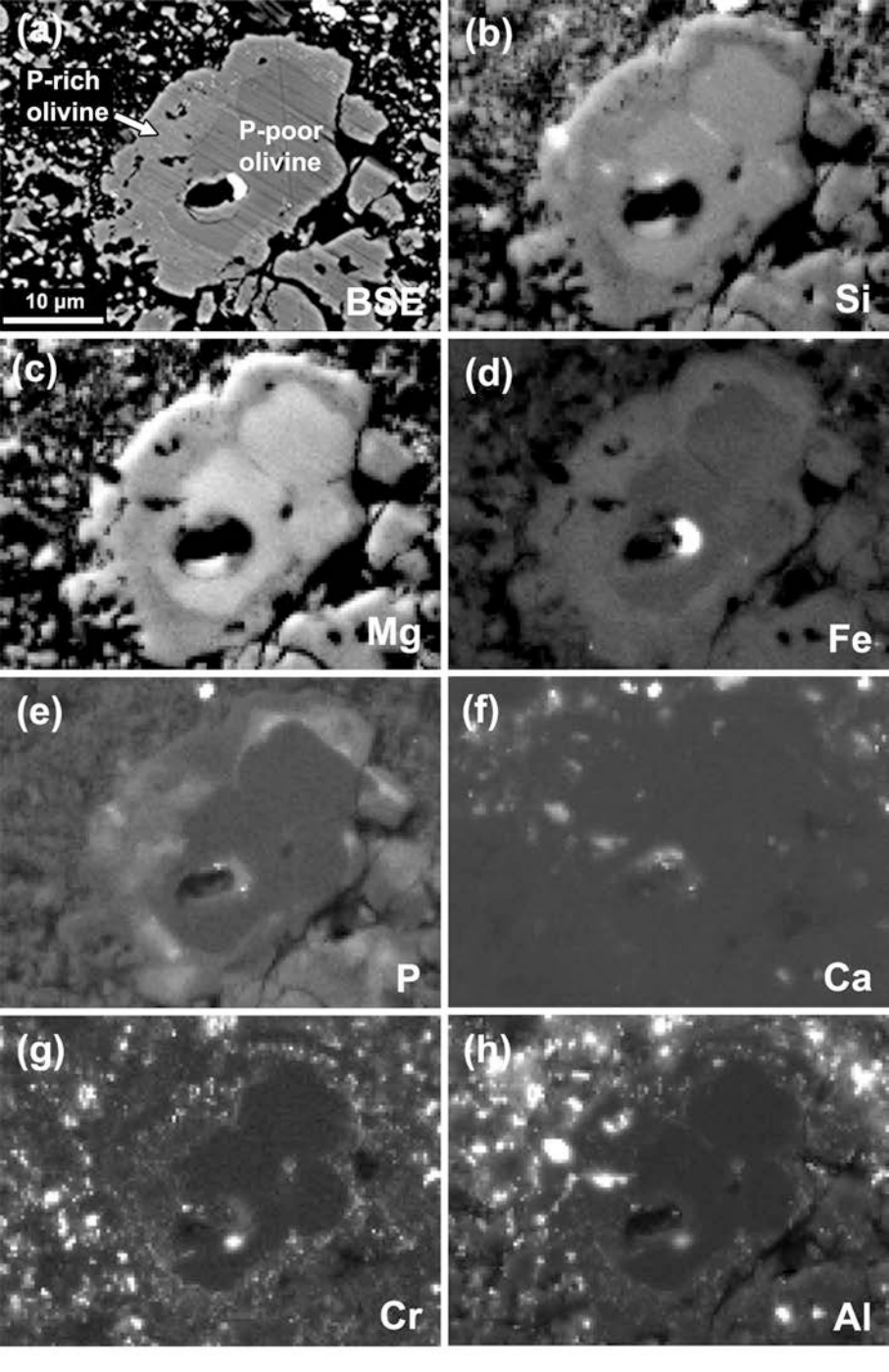
(a)
P-rich olivine
P-poor olivine
10 µm
BSE
(b)
Si
(c)
Mg
(d)
Fe
(e)
P
(f)
Ca
(g)
Cr
(h)
Al

Figure 4

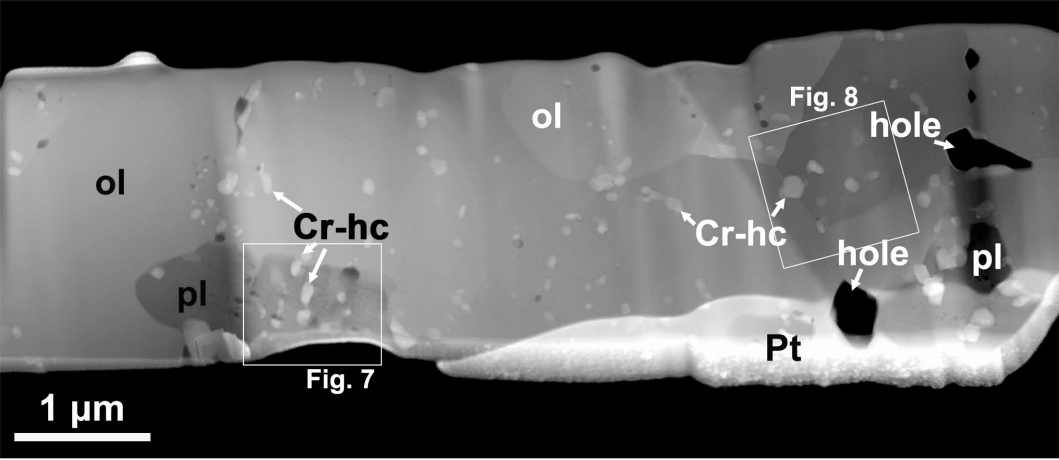

Figure 5

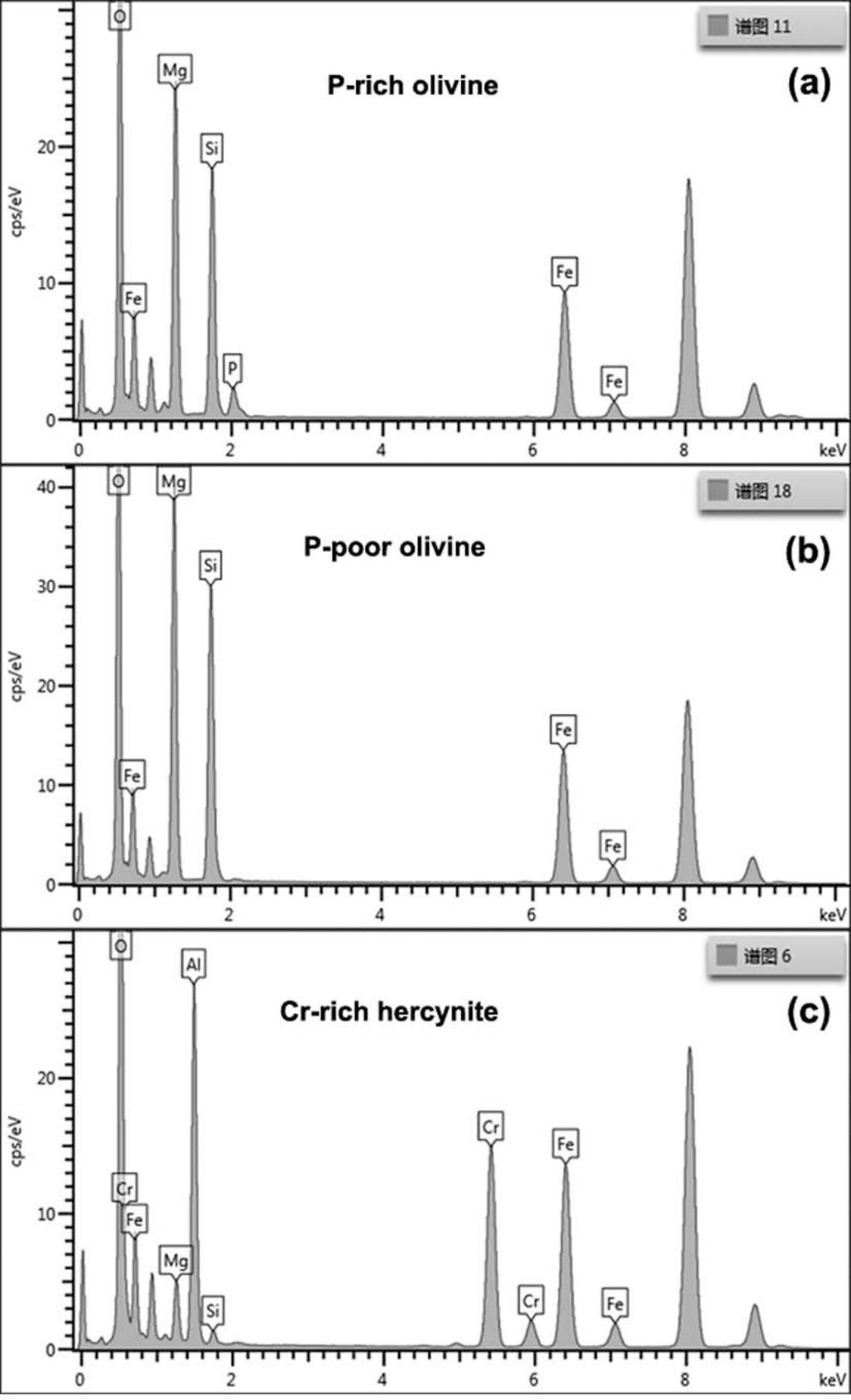
谱图 11
P-rich olivine
(a)
O
Mg
Si
Fe
P
Fe
Fe
cps/eV
keV
谱图 18
P-poor olivine
(b)
O
Mg
Si
Fe
Fe
Fe
cps/eV
keV
谱图 6
Cr-rich hercynite
(c)
O
Al
Cr
Fe
Mg
Si
Cr
Fe
Cr
Fe
cps/eV
keV

Figure 6

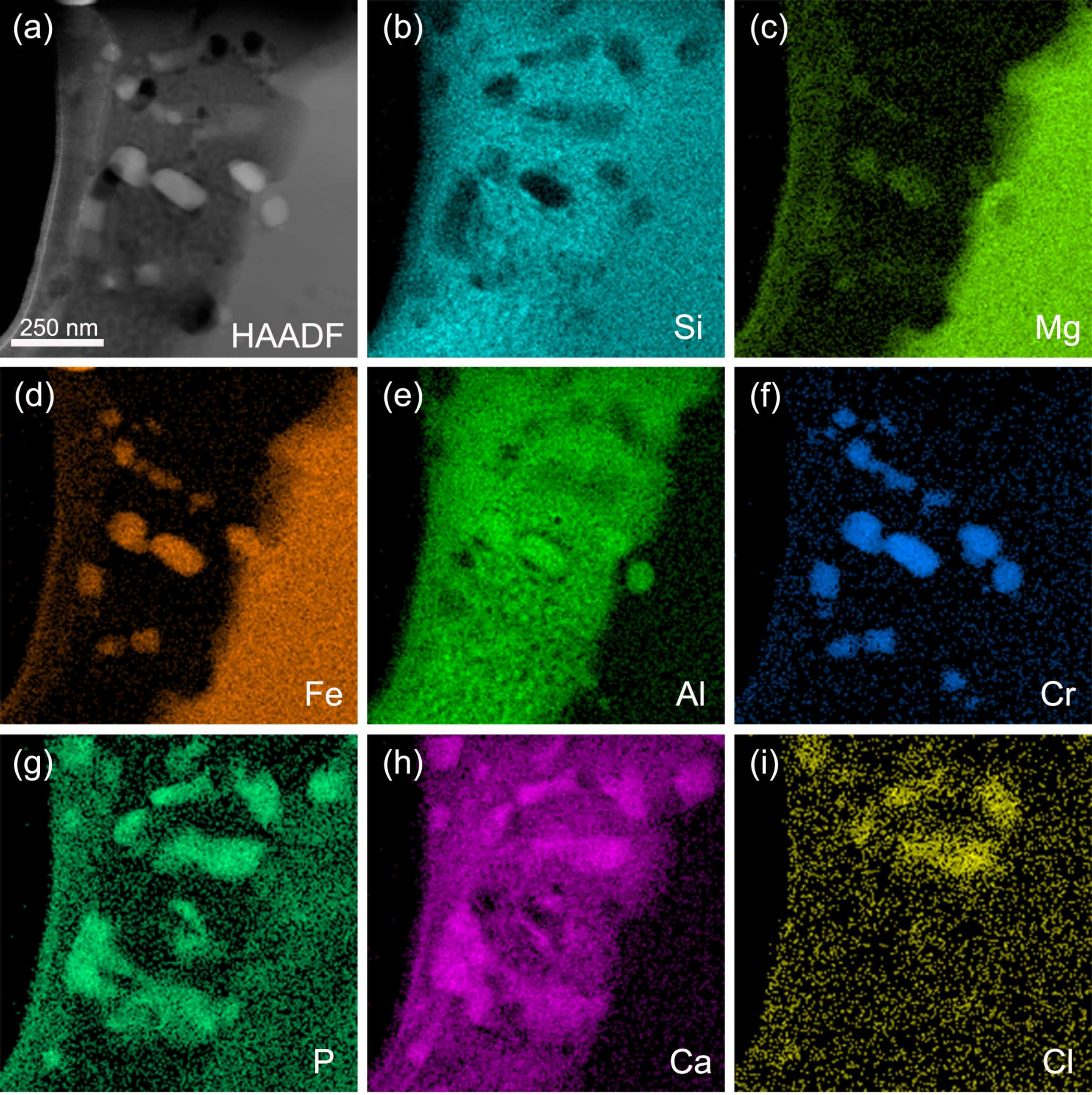

Figure 7

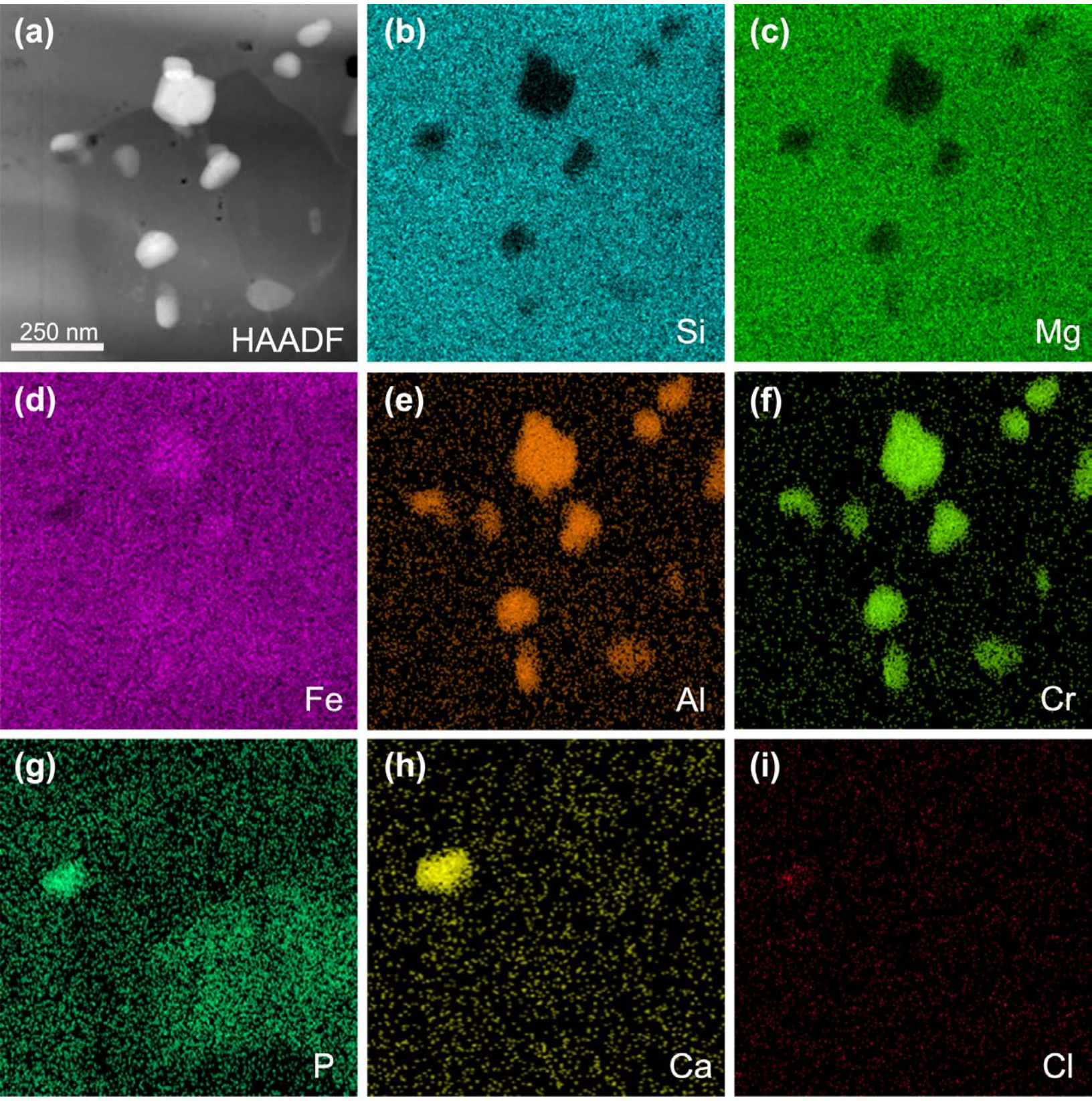

Figure 8